Resonant Response of Deep Convection to Surface Hot Spots

F. J. ROBINSON, S. C. SHERWOOD, AND Y. LI

Department of Geology and Geophysics, Yale University, New Haven, Connecticut

(Manuscript received 10 January 2007, in final form 2 May 2007)

ABSTRACT

Observations show substantial variations of the intensity of tropical and/or summertime deep convection on land that are not explained by standard measures of convective instability. One feature that distinguishes land surfaces is their heterogeneity. The possible importance of this is investigated here by calculating the response of a nonrotating atmosphere to localized, transient surface heating using both the linearized equations of motion and a cloud-resolving configuration of the Weather Research and Forecasting (WRF) numerical model with moist physics, each in 2D. Both models predict that the depth of the resulting surface heat low near storm center will be greatest for a particular horizontal scale of heating. The linear model reveals that this is a resonant scale determined by the product of the environmental buoyancy frequency, characteristic heating time scale, and thickness of the thermal boundary layer, and the resonance occurs when the aspect ratio of the applied heating matches the ratio of vertical and horizontal wavenumbers demanded by the dispersion relation for buoyancy (gravity) waves. For realistic conditions, the resonant horizontal scale is roughly 50 km. The numerical model indicates that other measures of convective intensity, such as updraft speed and storm height, are largely controlled by the depth of the heat low, despite the presence of conditional instability and the vigorous growth of moist convective plumes. Predictions here agree with reported observations of storm severity over islands of different sizes. These findings may help explain why observed geographical variations in storm intensity defy parcel theory and indicate that phenomena often attributed to parcel entrainment may instead be due largely to storm-scale dynamical constraints.

1. Introduction

Peak convective cloud-top heights and other measures of convective intensity vary markedly from region to region (e.g., Zipser et al. 2006). Such variations are traditionally ascribed to variations in deep moist instability [i.e., convective available potential energy (CAPE)], which determines the amount of potential energy available for conversion to updraft kinetic energy. While CAPE undoubtedly favors stronger convection, all other things being equal, it is clear from previous work that much of the observed variation, especially in the tropics, cannot be explained by CAPE. For example, updrafts in continental storms are sometimes an order of magnitude faster than those in maritime storms, while typical land–ocean CAPE differences are unimpressive (e.g., Jorgensen and Lemone 1989; Zipser and Lutz 1994). A recent study by Sherwood et al. (2004) found that Florida area cumulus heights responded roughly as expected to day-to-day changes in CAPE but that diurnal and regional height variations, which were at least as large, had nothing to do with CAPE (due in part to well-known mesoscale dynamical effects). Thus, while CAPE or other indices of moist instability may be useful predictors for regional forecasters, other important and regionally variable factors are clearly at work.

Several possibilities have previously been suggested. Midlevel moisture has been shown by many studies to affect convective development and was found by Sherwood et al. (2004) to have a strong influence on convective penetration that could not be explained by parcel theory for any entrainment rate. It has been suggested that a deeper mixed layer over continents will lead to broader updrafts with less entrainment (McCaul and Cohen 2002; Zipser 2003). Surface roughness, elevated terrain, and aerosol indirect effects may also enhance the strength of continental convection (Ekman et al. 2004; Souza et al. 2000).

Corresponding author address: F. J. Robinson, Department of Geology and Geophysics, Kline Geology Laboratory, P.O. Box 208109, Yale University, New Haven, CT 06520-8109.
E-mail: francis.robinson@yale.edu

DOI: 10.1175/2007JAS2398.1

Interest in this problem has been further aroused by the dramatic confirmation by recent satellite observations (Christian et al. 2003) of early findings that lightning is an order of magnitude more likely to occur over land than it is over ocean (Orville and Henderson 1986). As lightning production is thought to be controlled mainly by the strength of vertical updrafts, resolving why updrafts are so much stronger over land may largely explain the land–sea lightning contrast. Williams et al. (2004) documented a transition size range for islands over which there was a significant increase in storm electrification. The transition from maritime to continental lightning characteristics occurred for islands with areas between about 100 and 1000 km^2. The explanation given for this transition was based on a kinematic argument involving the amount of heated air available for driving the storm. Our study provides an alternative explanation for their findings and identifies a new factor contributing to the observed vigor of land-based storms.

Surface temperature and moisture heterogeneity (induced, e.g., by water bodies having high heat capacities surrounded by land) can significantly affect the organization and height of shallow convective layers (e.g., Avissar and Liu 1996; Roy and Avissar 2000; Roy et al. 2003). Based on numerical simulations with sinusoidally forced surface temperature variations, these authors reported that for forcing wavelengths of 5–10 km, circulations of a similar size form in the boundary layer. If the heating width was higher, say 20 km, two types of rolls formed: (i) circulations of similar size to the heating width and (ii) turbulent eddies a few kilometers in width. They suggested that these are the results of the horizontal pressure gradient and buoyancy fluctuations, respectively. However, they did not distinguish between the contributions of waves and convection to the flow.

Previous studies do not clearly determine whether any analogous effects might occur for deep convection, although Weaver (2004) found that deep convection could be triggered by forced shallow mesoscale circulations. Whether such effects could modulate storm heights, locations, or organization is even less clear. We show here that surface heating heterogeneities can indeed control the intensity of deep convective storms. Further, we propose that this behavior can be simply understood as a linear resonant response of the atmospheric fluid according to dry fluid dynamics, despite the nonlinearity and latent heating occurring in the real system. Our mechanism may apply to the aforementioned studies and predicts enhancement of storm severity generally by heterogeneity in the lower boundary.

The rest of this paper is set out as follows: First, we describe a linear model of a dry fluid with constant stratification and calculate its response to a localized heat source. Next, we present fully nonlinear numerical cloud simulations with moist physics, isolating similarities in the response to the localized heating. Finally, there is a discussion and a conclusion.

2. Linear model of a dry atmosphere

We begin our analysis by investigating the linear Boussinesq equations under the idealized conditions of no mean flow and no rotation. This will enable us to explore the fluid-dynamical aspects of the problem without the complications of moist physics and turbulence. The approach also permits an analytical solution not dependent on a large number of model details to be used as a starting point for understanding numerical simulations.

a. Model equations

The 2D linearized Boussinesq equations (Smith 1988; Walsh 1974), in the absence of mean flow and with no Coriolis force, are

$$u_t = -p'_x - \alpha u, \tag{1}$$

$$w_t = -p'_z + b - \alpha w, \tag{2}$$

$$b_t + N^2 w = B - \alpha b, \quad \text{and} \tag{3}$$

$$u_x + w_z = 0, \tag{4}$$

where u and w are the velocities in the horizontal (x) and vertical (z) directions, N is the buoyancy frequency, and α is the damping coefficient. The adiabatic part of the pressure field has been subtracted so that

$$p' = [p - \overline{p}(z)]/\rho_0, \tag{5}$$

and buoyancy b is defined (Ogura and Phillips 1962) as

$$b = g(T - T_0 + gz/c_p)/T_0, \tag{6}$$

where T, T_0, ρ_0, c_p, and g are the temperature, the constant temperature and density of the background state, the specific heat capacity at constant pressure, and the acceleration due to gravity, respectively.

As a localized heat source, we chose the simple case of applied heating that is Gaussian in the horizontal dimension, sinusoidal in time t, and exponential in the vertical:

$$B(x, z, t) = B_0 \exp\left[-\frac{x^2}{a_0^2} - \frac{z}{H} + i\left(\sigma t - \frac{\pi}{2} \right) \right], \tag{7}$$

where the constant

$$B_0 = \frac{gQ}{\rho_0 c_p T_0}, \tag{8}$$

and Q is the constant heating strength in units of watts per meter squared. The heating source (7) is defined by three parameters: the heating frequency σ, the horizontal half-width a_0, and the vertical-scale height H. The dynamics are governed by two parameters: N and α. The latter is set to a very small value (10^{-8} s^{-1}) so that the damping time scale is much longer than the time period of the applied heating (a few hours). The model domain is infinite in the x and semi-infinite in the z directions, and has a constant static stability (constant N).

b. Analysis

By doing a Fourier transform in x and t (we omit the prime symbol on pressure henceforth) and solving Eqs. (1)–(4) (see the appendix for further details), we obtain

$$\hat{p}(k, z, t) = \frac{\hat{B}(k, t)}{\overline{\sigma}[(1/H)^2 + \gamma^2]} \times \left[\frac{i}{H}\exp(-z/H) - \gamma \exp(i\gamma z)\right], \tag{9}$$

where

$$\hat{B}(k, t) = \exp(-k^2 a_0^2/4)\exp[i(\sigma t - \pi/2)] \tag{10}$$

and $\overline{\sigma} = \sigma - i\alpha$, with a similar expression for vertical velocity. The characteristic vertical wavenumber γ is defined as

$$\gamma^2 = \frac{k^2(N^2 - \overline{\sigma}^2)}{\overline{\sigma}^2} \approx \left(\frac{Nk}{\overline{\sigma}}\right)^2, \tag{11}$$

and the heating frequency $\sigma \ll N$ refers to a heating period of a few hours. Performing the inverse Fourier transform, evaluating at $x = 0$ and $z = 0$, excluding terms multiplied by α (which are all very small and do not affect the final result) and noting that the heating strength reaches a maximum at $t = \pi/2\sigma$, gives

$$p(x = 0, z = 0, t = \pi/2\sigma) = -B_0 f(N, \sigma, a_0, H), \tag{12}$$

where

$$f(s) = \frac{\sqrt{2}H}{\sigma} s \exp(s^2) E_i(1, s^2) \quad \text{and} \tag{13}$$

$$s = (a_0\sigma)/(2HN), \tag{14}$$

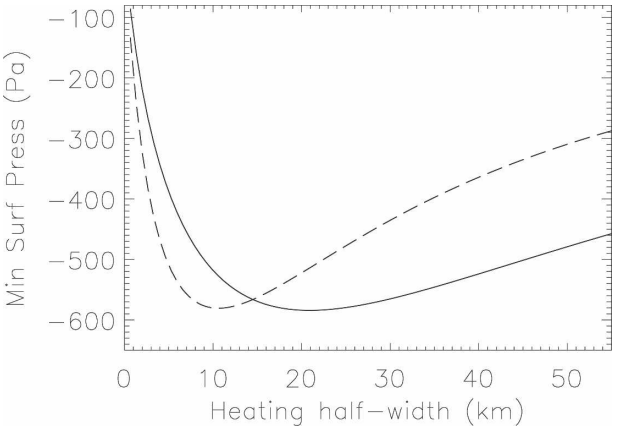

FIG. 1. Minimum surface pressure perturbation in the linear model solution (12) for two buoyancy frequency values $N = 0.006$ (dashed) and $N = 0.012$ s^{-1} (solid), plotted vs heating source half-width.

and the exponential integral is defined by

$$E_i(1, s^2) = \int_1^\infty \frac{\exp(-s^2 t)}{t}\, dt. \tag{15}$$

Figure 1 shows the strength of the heat low in the model solution $p(x = 0, z = 0, t = 45$ min) as a function of source half-width for two values of the stratification. In each case H equals 1 km and the heating period is 3 h (because of the sinusoidal time dependence of the heating function, the minimum pressure perturbation occurs at around one-quarter of the heating period, i.e., 45 min, just after the temperature reaches a maximum). These choices of H and t are motivated by the numerical model solutions presented in section 3. The two values of N correspond roughly to an observed tropical value and the value of an atmosphere with half the stratification. For each N there is a corresponding minimum, though that of the less stratified case occurs at a smaller value of a_0.

To locate this minimum analytically, we fix H, N, and σ and find the minimum surface pressure perturbation by solving

$$\frac{\partial f(s)}{\partial a_0} = \frac{\partial f(s)}{\partial s}\frac{\partial s}{\partial a_0} = 0, \tag{16}$$

which can be rewritten as

$$\frac{\partial f(s)}{\partial a_0} = \frac{\sqrt{2}H}{\sigma}[(1 + 2s^2)\exp(s^2)E_i(1, s^2) - 2]\frac{\sigma}{2HN} = 0, \tag{17}$$

the numerical solution of which is $s = 0.5$, implying that the pressure perturbation at the center reaches a mini-

mum when the critical source half-width a_c satisfies the relationship

$$\frac{a_c}{H} = \frac{N}{\sigma}. \tag{18}$$

c. Interpretation

The physical basis of this result can be understood by returning to the dispersion relation for internal gravity waves

$$\nu = N \frac{L_z}{(L_x^2 + L_z^2)^{1/2}}, \tag{19}$$

where ν is the gravity wave frequency, and L_x and L_z are the horizontal and vertical wavelengths (Holton 1992). As $L_x \gg L_z$, and gravity waves preferentially oscillate at the imposed heating frequency σ, this relation can be written as

$$\frac{\sigma}{N} \approx \frac{L_z}{L_x}. \tag{20}$$

When the ratio of the imposed vertical length scale (boundary layer depth, H) to the horizontal length scale (heating width, a_c) is equal to σ/N, gravity waves will propagate most efficiently.

In the linear model, the depth of the pressure low and the strength of the thermally direct time-dependent circulation are maximized for resonant combinations of vertical and horizontal forcing scales. To achieve this resonance, the ratio of these length scales must match that of vertical and horizontal wavelengths of buoyancy waves supported by the fluid medium at the forcing frequency. The strength of the response diminishes rapidly when the model is forced at horizontal scales that are too short because the profile of the applied vertical heating contains little energy at the correspondingly short vertical wavelengths demanded by the wave dispersion relation. To the extent that this model describes the behavior of the atmosphere, we may then expect certain length scales of heating to generate a stronger dynamical response.

A deep moist convective system is clearly much more complex: there is latent heating, moisture, and microphysics, and the flow is turbulent and characterized by advection and other nonlinear processes not included above. Thus while the above calculation may apply in a relatively straightforward way to shallow atmospheric flows of modest amplitudes that do not involve precipitation, it remains to be seen whether this calculation has any relevance to the behavior of deep moist convection. We now present tests of this.

3. Cloud-resolving model

The cloud-resolving simulations were computed using the Weather Research and Forecasting Model (WRF, version 2) model, which solves the fully compressible hydrodynamic (Navier–Stokes) equations (Wicker and Skamarock 2002). It uses a third-order-accurate Runge–Kutta scheme for the time integration, and second–sixth-order-accurate spatial discretization is available for the advection terms. Our setup is very similar to that in Robinson and Sherwood (2006, hereafter ROB06); the only difference is that we keep the model physics the same while varying the thermal forcing. To avoid unnecessary model complexity we used the simplest physics options: warm-rain Kessler microphysics (no ice), turbulent kinetic energy model, and no radiation scheme. This retains the nonlinearity and latent heating characterizing real storms while avoiding variations among the simulations due to differences in cloud glaciation.

All simulations used a 2D version of the model running on local machines. The model domain was 600 km (1200 grid points with a grid spacing of 500 m) in the across-line direction with open sidewalls and 30 km (200 grid points) in the vertical direction with a stress-free impenetrable top and bottom. In ROB06 we showed that horizontal resolutions of 250 and 500 m produce very similar results and that it is the vertical resolution that is most important. The vertical grid spacing varied from about 100 m at the ground to about 50 m in the tropical tropopause layer (TTL) and increased smoothly up to the top. It was designed to resolve gravity waves in all layers (the grid was similar to that shown in ROB06 with twice finer resolution near the ground). The choice of grid was justified by our previous sensitivity study and is in line with findings from Lane and Knievel (2005). The difference between our findings and those of Bryan et al. (2003) may be due to the higher-order numerics used in the WRF model (Lane and Knievel 2005). As the top was impenetrable, the uppermost 6 km was a viscous damping region designed to reduce reflections of gravity waves at the top.

a. Model initialization

We simulated the growth of convective storms in a conditionally unstable subsaturated environment specified from a mean June–August (JJA) tropical sounding having a CAPE of about 500 J kg^{-1}. This sounding was identical to that used by ROB06, except that tropospheric relative humidities were capped at 99% to eliminate the slight supersaturation previously present at the top of the mixed layer. This sounding had a tropospheric static stability of roughly 0.012 s^{-1}, hence our

choice of this in the linear model. Latent heat of fusion was excluded from the computation of CAPE. (Note: ROB06 mistakenly included the latent heat of fusion in their computation of CAPE, even though the simulations themselves did not include freezing of condensate; the actual CAPEs attained were about 1000 J kg^{-1} less than reported.)

To test the predictions of the linear model we wanted to concoct an initial sounding with a substantially different buoyancy frequency. Deep convection would only develop in a comparable way if the moist stability (CAPE) and relative humidity were similar to before. To satisfy all requirements, we reduced the surface temperature by 20 K and adjusted the sounding temperature at each model level so that the buoyancy of a parcel lofted pseudoadiabatically from near the surface was the same as before. This preserves not only the CAPE but also the shape of the CAPE. The water vapor mixing ratios were then specified to yield the same relative humidity as before on each model level. Since the resulting sounding had a lot less moisture in it but the same CAPE, the new lapse rate was much closer to dry adiabatic and N decreased to approximately 0.006 s^{-1} above the boundary layer. Figure 2 shows the run of the potential temperature of the two soundings. The cold point in the colder sounding was at nearly the same pressure as before, but the corresponding altitude dropped to 14 km compared with the original 16.5 km because of thermal contraction. The stratospheric stability was the same as in the warmer sounding.

Note because in the WRF model the phase speed at the open boundary is fixed at 25 m s^{-1}, and because the horizontal phase speed of gravity waves is linear in N, when we halved the stability we also halved the phase speed at the open boundary (parameter *cb* in the WRF model). Sensitivity tests indicated that this only had a minimal effect on the results of interest.

b. Thermal forcing

To obtain a smoothly developing convective system, we added a surface perturbation T' to the temperature T at the lowest model level, $T'/2$ to the temperature at the second lowest level, and $T'/4$ at the third lowest level, where

$$T' = A_0 \exp[-(x - 1/2)^2]tT, \tag{21}$$

where A_0 is the amplitude of the temperature perturbation and the horizontal distance x is scaled by the total width of the heating source and positioned in the center of the domain (x is between 0 and 1). When time t exceeds a certain value then $T' = 0$. This cutoff time

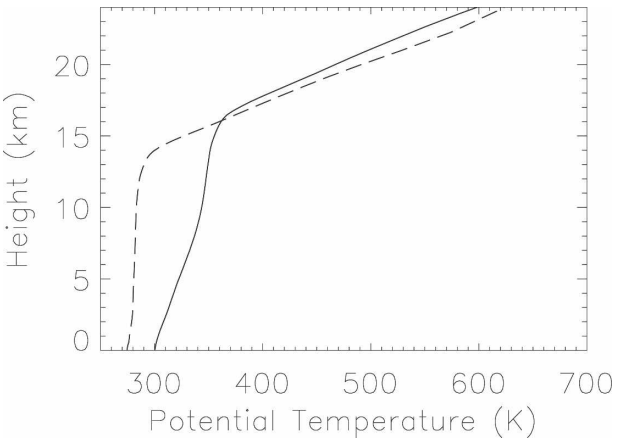

FIG. 2. Original (N; solid line) and cold ($N/2$; dashed line) soundings.

and A_o are chosen so that the maximum temperature perturbation is up to about 10 K spread over 1–2 h. To minimize convective effects at the open sidewalls, the perturbation is set to zero outside of the heating region.

For each of our two initial states, we ran a series of simulations spanning a range of source half-widths from 2 to 50 km. Each run was only for a few hours' duration, since the main goal is to observe the strength of the strongest updrafts, which occur early during the life of the simulated storm.

c. Comparing WRF model with the linear model

While we are free in the linear model to arbitrarily vary the parameters N, σ, H, and a_0, not all of these can be set by fiat in the more realistic WRF model. We described above our method for varying N and a_0, the latter being the more straightforward. We diagnosed the scale height H and half-width a_0 for each simulation by examining the difference in the temperature distribution just prior to the rapid growth of deep convection (defined as the time at which the CAPE reaches a maximum as shown in Fig. 3), versus that in the initial sounding. Unsurprisingly the diagnosed a_0 was essentially the same as that of the applied heating. We found, however, that no matter how we put heat into the numerical model (provided it was confined near the surface as would happen due to daytime solar absorption), we ended up with $H \approx 1$ km (see Fig. 4) due to the action of small-scale turbulent transport. This scale height remained indifferent even to our dramatic change of initial sounding. Thus, we were unable to test the response of the numerically simulated storms to changes in this linear model parameter.

A similar problem exists for the heating time scale. In the linear model, the heating strength reaches a maximum at the time τ defined by

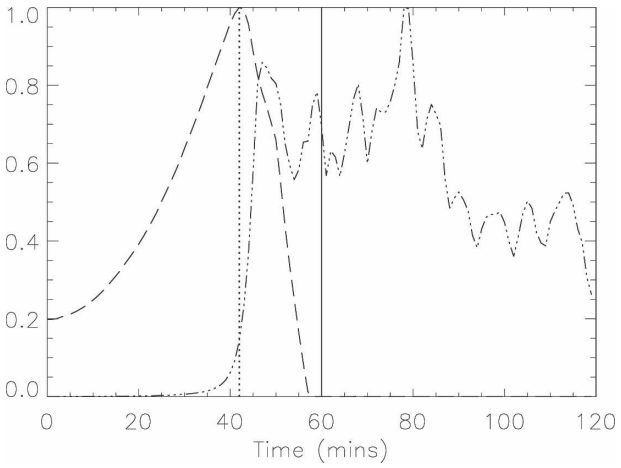

FIG. 3. Time evolution of local CAPE (dashed line) averaged over the full heating width and maximum vertical velocity (triple-dot–dashed line) in the control simulation (a_0 = 25 km and N = 0.012 s^{-1}) for a typical convective event. Both are scaled by their maximum values, which are 2560 J kg^{-1} and 40 m s^{-1}, respectively. The dotted vertical line marks the time τ at which the pressure minimum and depth of thermal boundary layer are computed, while the solid vertical line marks the start of the 1-h time integration for the computation of turbulent statistics (sensible heat flux, updraft speed, and cloud-top height).

$$\tau = \pi/2\sigma. \tag{22}$$

To be consistent with the measurement of H, in the WRF model we define τ as the time at which the CAPE reaches a maximum. While the thermal forcing can be applied either slowly or rapidly, the convection tended to develop at a relatively similar time into the simulation (τ was always about 40–50 min); this timing was probably determined by details of the initial profile as well as growth rate of initial fluctuations in the model state.

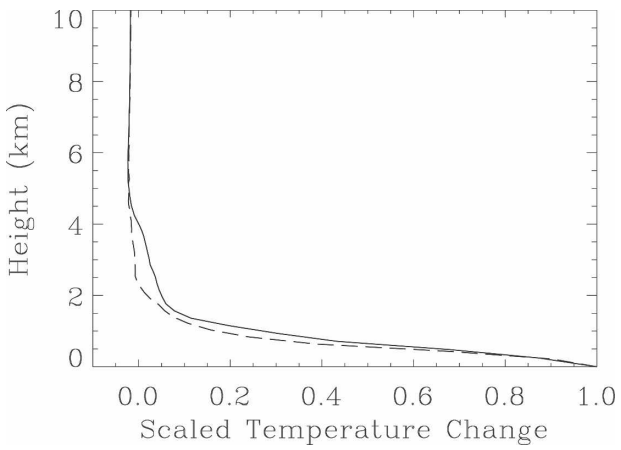

FIG. 4. Change in the background temperature divided by the maximum change, $\Delta T/(\Delta T)_{max}$, between the start of a typical simulation and the time of maximum CAPE for the original [N, $(\Delta T)_{max}$ = 8.5 K, and a_0 = 25 km; solid line] and cold [N/2, $(\Delta T)_{max}$ = 6 K, and a_0 = 18.5 km; dashed line] sounding. In each case the temperature T has been averaged over the heated area. Even though we have specified a_0, the actual value has little effect on the shape of the temperature profile that develops with each sounding.

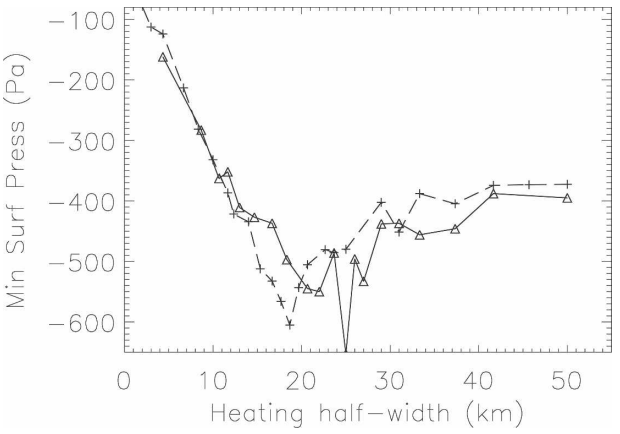

FIG. 5. Minimum surface pressure perturbation at the time of maximum CAPE for WRF simulations initiated with original (N; solid line) and cold (N/2; dashed line) soundings, plotted vs heating source half-width.

d. Preconvective surface pressure

To be consistent with the diagnosis of H, we compared the WRF behavior with that of the simple model by noting the surface pressure perturbation at time τ.

Both the minimum surface pressure perturbation and the horizontally averaged surface pressure perturbation were computed for each simulation, with the results for the minimum pressure perturbation for the two soundings plotted in Fig. 5. The horizontally averaged and minimum values behave in the same way over time.

Comparing Figs. 5 and 1 shows that the pressure perturbation field in the WRF model shares a number of features in common with the linear model. Though there is significant noise, particularly in the warmer sounding, there is a clear shift in the location of the minimum when the stability is halved. For the original (N) sounding the minimum is at about 25 km, while for the colder (N/2) sounding it is at about 18 km. The curvature is similar to the linear case, in that there is a sharp drop toward zero in the magnitude of the surface pressure perturbation for subresonant values of a_0 but only a gradual decline for forcings broader than the resonant value. This agreement is remarkable given that in the WRF simulation the pressure perturbation is measured at a time when the flow is significantly nonlinear with maximum point velocities of a 1–10 m s^{-1}. A series of runs were also performed for a dry atmosphere

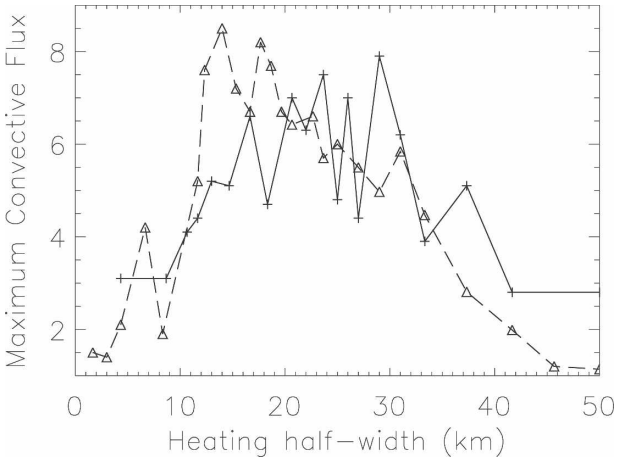

FIG. 6. Peak convective heat flux (kg m^{-2} s^{-1} K) simulated by WRF vs heating source half-width, with original (N; solid line) and cold ($N/2$; dashed line) soundings.

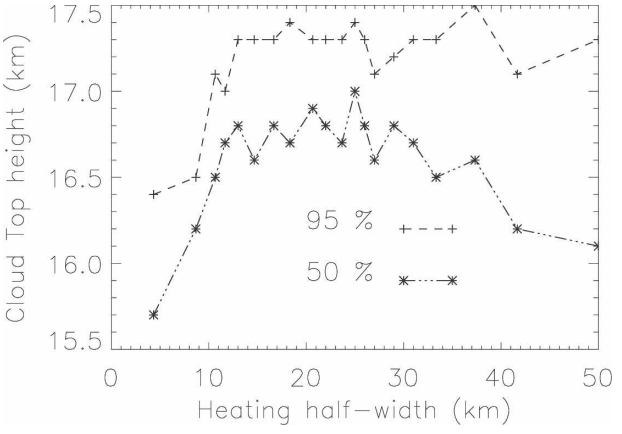

FIG. 7. WRF-simulated 50th- and 95th-percentile-high cloud-top heights vs heating source half-width for the original (N) sounding.

by setting the mixing ratio to zero in the initial sounding. In that case the optimum heating width a_c and scale height H were almost the same as those in the moist simulations.

e. Convective vigor

1) SENSIBLE HEAT FLUX

One measure of convective vigor is the upward turbulent sensible heat flux, which can be defined as $\overline{\rho w' \theta'}$ where ρ, w, and θ are the density, vertical velocity, and potential temperature, respectively. The fluctuating parts were computed as $w' = w - \overline{w}$ and $\theta' = \theta - \overline{\theta}$, so that the mean flow has been subtracted and the flux represents the net effect of resolved turbulent eddies. The overbar represents an average over all the points for one hour of turbulent developed convection for which the cloud water content is greater than zero. The start time for this averaging was the first time the plumes had enough momentum to squash the stratospheric isentropes together so the maximum $\partial\theta/\partial z$ occurred in the TTL.

Figure 6 is a plot of the maximum sensible heat flux versus heating half-width for the two different input soundings. The peak response lies somewhere between about 20 and 30 km for the warm sounding and between 10 and 20 km for the cold sounding. This is a very similar range to that for surface pressure perturbation, suggesting that the pressure low may control the vigor of the moist convective response.

2) CLOUD TOPS AND UPDRAFT SPEEDS

A more observable measure of convective strength is cloud-top height. By examining all the grid points between 14- and 17-km altitude for which the integrated cloud water content was at least 0.02 kg m^{-2} (approximately the level of unit optical depth) over one hour of the convective life cycle, we computed two measures of peak cloud height. Figures 7 and 8 show the 95th- and 50th-percentile cloud-top heights plotted against a_0 for our standard N and $N/2$ cases. The results are somewhat sensitive to the measure chosen, and because of the complexity of the simulated fields, the position of the peak response could not be as easily seen as in the dynamical fields. Nonetheless the general picture is similar to that of the dynamical fields, with a broad maximum of cloud height obtained for half-widths between about 15–35 and 5–20 km for the N and $N/2$ cases, respectively.

The vertical velocities of the strongest updrafts are another measure of prime importance for cloud microphysics and electrification. Because of the complicated velocity structure, the highest ascent rate attained at one time step and grid point was not a suitable measure.

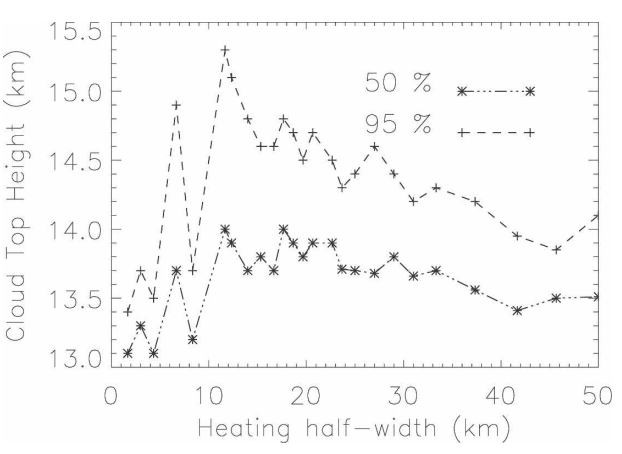

FIG. 8. As in Fig. 7 but for the cold ($N/2$) sounding.

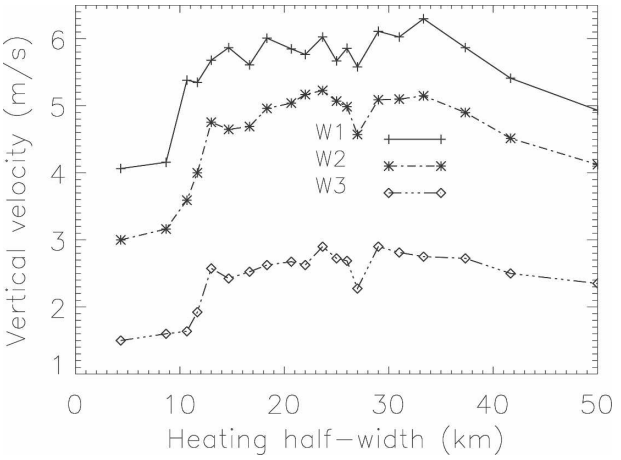

FIG. 9. Three metrics (see text for explanation) for WFR-simulated vertical velocity vs heating source half-width for the original (N) sounding. W3 has been divided by 8 for plotting.

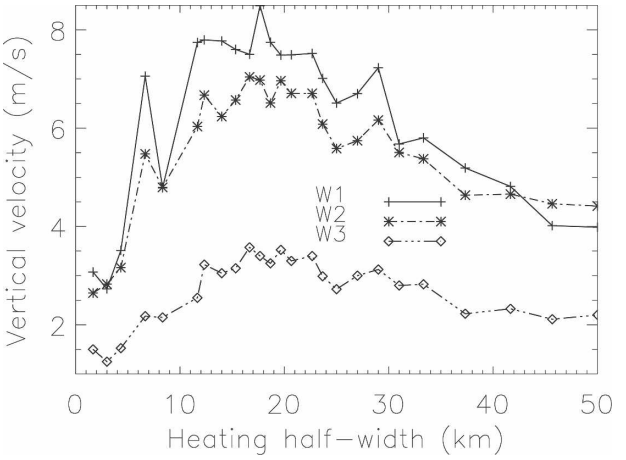

FIG. 10. As in Fig. 9 but for the cold ($N/2$) sounding.

We instead computed three integral measures of vertical velocity extremes: $\overline{w^3}$, $\overline{w^2}$, and the 95th percentile of w. The overbars denote averaging over time (1 h) and space (all the points lying below 18 km at which the cloud water content is greater than zero). The results for the standard N case are plotted in Fig. 9 and for the $N/2$ sounding in Fig. 10. In both plots, W1 = $\overline{w^3}^{1/3}$, W2 = $\overline{w^3}^{1/2}$, and W3 = 95th percentile of w (divided by 8 to fit on the same axes as the other velocities). The results are more robust than those for cloud height, and they are consistent with the other fields, with peak responses occurring for half-widths from about 15 to 35 km for the standard sounding, and from about 5 to 25 km for the $N/2$ sounding. The sharper peak in w^3 compared with w^2 is probably a result of strong thin updrafts that come from the thin horizontal range over which the surface pressure perturbation peaks for the colder sounding.

As lightning production is thought to depend on vertical updraft speed, these results suggest the predominance of lightning over and above a certain range of island areas could be explained by the propagation of internal gravity waves and the height of the thermal boundary layer established prior to convective onset. Note that the pressure minimum in the more stable sounding has a much broader trough than the curve for the sounding with lower N. This may explain why the updraft skewness w^3 and 95th-percentile cloud-top height have much better defined peaks for the cold ($N/2$) sounding.

f. Vertical scale of convective eddies

Previous studies have often invoked the idea that thicker boundary layers (prevalent over continents) will produce fatter updrafts that will be slowed down less by entrainment (e.g., McCaul and Cohen 2002; Zipser 2003). This motivated us to look at characteristic eddy sizes in our simulations. We estimated these by computing the spatial autocorrelation of the w' field as a function of vertical and horizontal distance in the domain, defining the eddy size as the distance at which field autocorrelation falls to 0.5. The calculation included only data from model time steps for one hour of turbulent developed convection, within $2a_0$ of the center of heating in either horizontal direction, and at least 4 km above the surface and 4 km below the tropopause. This emphasizes deep convective up- and downdrafts while minimizing the impact of lateral boundary effects, stratospheric waves, and boundary layer turbulence.

Figure 11 shows the estimated eddy size versus source half-width for the original (N) sounding. Eddies

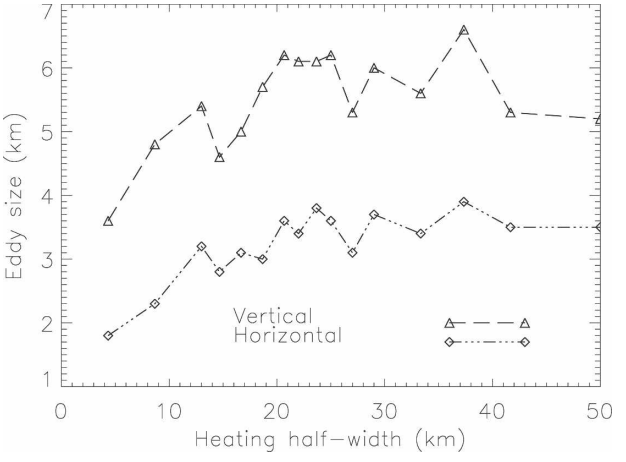

FIG. 11. Estimated eddy size (see text) vs heating source half-width in the WRF simulation with original (N) sounding.

became larger as the convection was forced at larger scales, but reached a plateau as the forcing half-width approached 50 km. The vertical and horizontal sizes scaled together at a ratio of about 3:2, as might be expected for quasi-spherical thermals. The increasing size of the eddies suggests that entrainment effects may also have played a role in governing the intensity of the response of w to the different forcings. This entrainment effect is probably secondary to that of the wave dynamics, however, since the linear model has no plumes or entrainment, yet produced essentially the same result. Previous studies may have erroneously interpreted a correlation between updraft strength and fatter drafts as entirely causative, when the two aspects could to a large extent have been mutual effects of dynamical changes. A similar analysis of the simulation initiated with the cold sounding (not shown) reveals eddies about 30% bigger and updrafts about 30% stronger than in the original sounding.

Interestingly, the thermal boundary layer height (see Fig. 4) did not change in any of the experiments. Thus, previous suggestions that updraft width might be controlled by boundary layer thickness do not tell the whole story. The flip side of this is that changes in boundary layer thickness may alter storm strength dynamically, independent of any updraft dilution effect, by changing the resonant scale. Also, numerical experiments in which heating is initialized by a warm bubble introduce an additional vertical length scale that complicates matters and may interact with the other two scales. While we have not performed a more detailed analysis to explain what controls eddy size, mesoscale forcing clearly must play a role alongside any played by the thickness of the boundary layer.

4. Discussion and conclusions

Previous studies have shown that boundary layer convection prefers certain scales that are not simply those of the boundary layer thickness itself (Avissar and Liu 1996; Roy and Avissar 2000; Roy et al. 2003). Others have shown that deep convection can be organized by waves, including self-generated ones (e.g., Mapes 1993; Thompson et al. 1979). Our results indicate wave modulation is a function not only of the horizontal organization of convection, but also its strength, even for deep convection in a conditionally unstable environment.

Our results have several implications. Nontrivial variations in convective intensity can result from mesoscale thermal forcing without changing the thermodynamic sounding (thus the CAPE or boundary layer thickness). This highlights the limitations of parcel theory in fully explaining updraft strengths and convective severity. The intensity changes are reflected in peak updraft and downdraft speeds, heat flux, and cloud-top height. They would presumably affect electrification and microphysical processes too, although we did not investigate this directly.

While the weakness of maritime updrafts has long indicated the limited relevance of nonentraining parcel theory, it is popular (e.g., McCaul and Cohen 2002; Zipser 2003) to rescue parcel theory by invoking strong updraft dilution through entrainment to explain the vastly reduced updraft speeds often seen. While this is no doubt important, we question whether this is the only or even the primary explanation for geographic variations in intensity. We find (not shown) that local vertical accelerations in WRF often differ dramatically from those anticipated from hydrostatic parcel buoyancy due to dynamical pressure perturbations. The similarity reported here between the responses of the linear Boussinesq model and the WRF numerical model to different forcings indicates that this behavior was controlled primarily by wave dynamics, even though stronger updrafts indeed tended to be wider. Parcel theory is irrelevant to the linear model.

The role of wave dynamics may be understood as a resonant interaction between the heating and the medium. Convection is well known to produce "gravity" (buoyancy) waves, and indeed cannot proceed without doing so: large-scale motions (including upper-level divergence and surrounding subsidence) must accompany convective growth and latent heat release, initiating waves. The key components of the resonance are shown in Fig. 12. Convection that is forced in a way that optimizes the ability of the atmosphere to accommodate this process will be stronger.

The linear dispersion relation (11) for short-period waves implies a particular horizontal scale a_c, given a heating time scale $2\pi/\sigma$ and a vertical scale H. The latter two scales appear to be set by the rate of deep convective development and the thickness of the shallow thermal boundary layer, respectively, in ways that are robust to the forcing and to some aspects of the initial sounding. Because the thermal perturbation is exponential in z rather than harmonic, it contains a spread of vertical wavenumbers. The resonant response occurs in a peak that is correspondingly broad with respect to the horizontal forcing scale.

Realistic parameter and static stability values for the tropical atmosphere determine a resonant horizontal scale of order 50 km. Because the boundary layer thermal perturbation decays smoothly with height, it lacks vertical wavenumbers much higher than the peak one, $1/H$, but projects onto all of those lower than $1/H$. As a

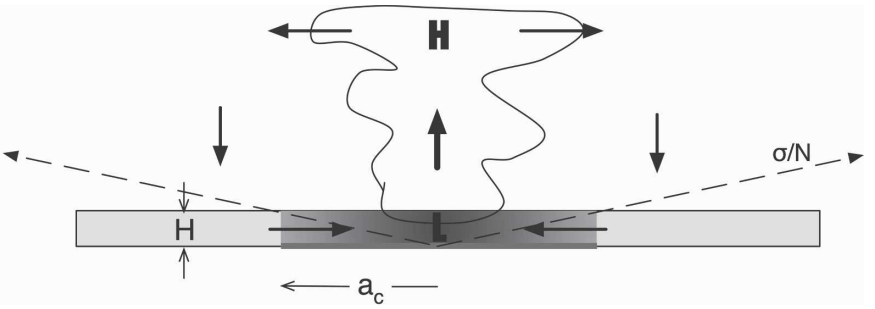

FIG. 12. Main components of the resonant response mechanism. The applied heating at the base (solid horizontal line) causes thermal expansion, creating a high aloft and evacuating mass from above the boundary layer, in turn causing a "heat low" or pressure minimum (L) at the surface. Air is drawn toward this heat low, but continuity demands an equivalent nearby subsidence. This complete circulation is most easily driven (resonant) when the ratio of the thermal boundary layer depth H to the width of the heated surface a_c is equal to the ratio of the vertical to horizontal wavelength of internal gravity waves supported by the atmosphere [$\approx\sigma$/N according to the standard short-period dispersion relation, Eq. (11)].

result, the response weakens rapidly for forcing scales below optimum but only slowly for scales broader than the optimum. This behavior is confirmed by the observation of Williams et al. (2004) that electrification is significantly reduced in storms forming over islands less than a few hundred square kilometers in size. The mechanism is also a likely factor in explaining the intensity of the well-known "Hector" storm, which forms north of Australia over a pair of closely spaced islands of approximate combined size 50 × 100 km and which routinely exceeds 19 km in height. We anticipate that the ability of volcanic eruptions and nuclear blasts to reach into the stratosphere will also be significantly affected by the horizontal extent of heating, although the impulsive nature of the heat source may require a full spectral solution of the linearized equations. This is straightforward but would require a numerical treatment.

One cautionary note is that because of the large number of simulations required, we have not yet tested this mechanism in three-dimensional simulations. While the same dynamics surely applies in three dimensions, their importance relative to other factors such as draft entrainment could be altered. Also, we have compared a linear model with periodic time forcing with a numerical calculation of a single event; possible problems with this have not been studied carefully, but may not be too important in light of the consistent behavior between the two calculations.

Another interesting result worth mentioning is that the WRF updraft speeds and parcel sizes were about 30% higher for a colder (by ~20°C) sounding even though the atmospheric soundings had the same profiles of buoyancy (thus CAPE) and relative humidity. If this result is robust, it implies that in different climates, the differing dry static stability may lead to different convective strength for dynamical reasons in addition to whatever microphysical effects the differing water vapor mixing ratios might have. It is possible that this temperature sensitivity is due to differences in the role of latent heating and cooling at the edges of the convective drafts, but we have left this topic for future research.

Acknowledgments. R. Smith provided valuable assistance for this work, including some of the mathematical development; SCS also thanks E. Williams and E. Zipser for useful discussions. This work was supported by NASA Grant NNG04GH66G and NSF Grants ATM-0134893 and ATM-0531212.

APPENDIX

Derivation of Eq. (9)

Fourier transform (FT) of Eqs. (1)–(4) in x and t (dropping the primes on p) produces

$$is\hat{u} = -ik\hat{p} - \alpha\hat{u}, \tag{A1}$$

$$is\hat{w} = -\hat{p}_z + \hat{b} - \alpha\hat{w}, \tag{A2}$$

$$is\hat{b} + N^2\hat{w} = \hat{B} - \alpha\hat{b}, \quad \text{and} \tag{A3}$$

$$ik\hat{u} + \hat{w}_z = 0, \tag{A4}$$

where the "hats" denote Fourier-transformed quantities, and s and k are the temporal and spatial wavenumbers. Algebraic manipulation of Eqs. (A1)–(A4) followed by an inverse FT in time gives

$$\hat{w}_{zz} + \gamma^2\hat{w} = \frac{k^2}{\bar{\sigma}^2}\hat{B}(k, z, t), \tag{A5}$$

where $\gamma^2 = k^2(N^2 - \overline{\sigma}^2)/\overline{\sigma}^2$ and $\overline{\sigma} = \sigma - i\alpha$. Solving the ODE and employing the appropriate boundary conditions produces

$$\hat{w}(k, z, t) = \frac{k^2\hat{B}(k, t)}{\overline{\sigma}^2(1/H^2 + \gamma^2)}[\exp(-z/H) - \exp(i\gamma z)], \tag{A6}$$

where

$$\hat{B}(k, t) = \exp(-k^2a_0^2/4)\exp[i(\sigma t - \pi/2)]. \tag{A7}$$

Using the relationship

$$\hat{p}(k, z, t)\frac{\overline{\sigma}}{ik^2}w_z, \tag{A8}$$

which can be found by combining Eqs. (A1) and (A4), and then inserting Eq. (A6) into Eq. (A8) gives

$$\hat{p}(k, z, t) = \frac{\hat{B}(k, t)}{\overline{\sigma}[(1/H)^2 + \gamma^2]} \times \left[\frac{i}{H}\exp(-z/H) - \gamma\exp(i\gamma z)\right]. \tag{A9}$$

REFERENCES

Avissar, R., and Y. Liu, 1996: Three-dimensional numerical study of shallow convective clouds and precipitation induced by land surface forcing. *J. Geophys. Res.,* **101,** 7499–7518.

Bryan, G., J. Wyngaard, and J. Fritsch, 2003: Resolution requirements for the simulation of deep moist convection. *Mon. Wea. Rev.,* **131,** 2394–2416.

Christian, H. J., and Coauthors, 2003: Global frequency and distribution of lightning as observed from space by the Optical Transient Detector. *J. Geophys. Res.,* **108,** 4005, doi:10.1029/2002JD002347.

Ekman, A. M. L., C. Wang, J. Wilson, and J. Strom, 2004: Explicit simulations of aerosol physics in a cloud-resolving model: A sensitivity study based on an observed convective cloud. *Atmos. Chem. Phys.,* **4,** 773–791.

Holton, J. R., 1992: *An Introduction to Dynamic Meteorology.* 3d ed. Academic Press, 511 pp.

Jorgensen, D. P., and M. A. LeMone, 1989: Vertical velocity characteristics of oceanic convection. *J. Atmos. Sci.,* **46,** 621–640.

Lane, T., and J. Knievel, 2005: Some effects of model resolution on simulated gravity waves generated by deep, mesoscale convection. *J. Atmos. Sci.,* **62,** 3408–3419.

Mapes, B. E., 1993: Gregarious tropical convection. *J. Atmos. Sci.,* **50,** 2026–2037.

McCaul, E. W., and C. Cohen, 2002: The impact on simulated storm structure and intensity of variations in the mixed layer and moist layer depths. *Mon. Wea. Rev.,* **130,** 1722–1748.

Ogura, Y., and N. Phillips, 1962: Scale analysis of deep and shallow convection in the atmosphere. *J. Atmos. Sci.,* **19,** 173–179.

Orville, R. E., and R. Henderson, 1986: Global distribution of midnight lightning: September 1977 to August 1978. *Mon. Wea. Rev.,* **114,** 2640–2653.

Robinson, F., and S. Sherwood, 2006: Modeling the impact of convective entrainment on the tropical tropopause. *J. Atmos. Sci.,* **63,** 1013–1027.

Roy, S., and R. Avissar, 2000: Scales of response of the convective boundary layer to land surface heterogeneity. *Geophys. Res. Lett.,* **27,** 533–536.

——, C. Weaver, D. S. Nolan, and R. Avissar, 2003: A preferred scale for landscape forced mesoscale circulations? *J. Geophys. Res.,* **108,** 8854, doi:10.1029/2002JD003097.

Sherwood, S. C., P. Minnis, and M. McGill, 2004: Deep convective cloud top heights and their thermodynamic control during CRYSTAL-FACE. *J. Geophys. Res.,* **109,** D20119, doi:10.1029/2004JD004811.

Smith, R. B., 1988: Linear theory of stratified flow past an isolated mountain in isosteric coordinates. *J. Atmos. Sci.,* **45,** 3889–3896.

Souza, E. P., N. O. Rennó, and M. A. F. Silva Dias, 2000: Convective circulations induced by surface heterogeneities. *J. Atmos. Sci.,* **57,** 2915–2922.

Thompson, R. M., Jr., S. W. Payne, E. E. Recker, and R. J. Reed, 1979: Structure and properties of synoptic-scale wave disturbances in the intertropical convergence zone of the eastern Atlantic. *J. Atmos. Sci.,* **36,** 53–72.

Walsh, J., 1974: Sea breeze theory and applications. *J. Atmos. Sci.,* **31,** 2012–2026.

Weaver, C. P., 2004: Coupling between large-scale atmospheric processes and mesoscale land–atmosphere interactions in the U.S. Southern Great Plains during summer. Part I: Case studies. *J. Hydrometeor.,* **5,** 1223–1246.

Wicker, L., and W. Skamarock, 2002: Time-splitting methods for elastic models using forward time schemes. *Mon. Wea. Rev.,* **130,** 2088–2097.

Williams, E., T. Chan, and D. Boccippio, 2004: Islands as miniature continents: Another look at the land-ocean lightning contrast. *J. Geophys. Res.,* **109,** D16206, doi:10.1029/2003JD003833.

Zipser, E. J., 2003: Some views on "hot towers" after 50 years of tropical field programs and two years of TRMM data. *Cloud Systems, Hurricanes, and the Tropical Rainfall Measuring Mission (TRMM), Meteor. Monogr.,* No. 51, Amer. Meteor. Soc., 49–58.

——, and K. R. Lutz, 1994: The vertical profile of radar reflectivity of convective cells: A strong indicator of storm intensity and lightning probability? *Mon. Wea. Rev.,* **122,** 1751–1759.

——, D. J. Cecil, C. T. Liu, S. W. Nesbitt, and D. P. Yorty, 2006: Where are the most intense thunderstorms on earth? *Bull. Amer. Meteor. Soc.,* **87,** 1057–1071.